TU Delft

Delft University of Technology

Incompatibility stress at inclined grain boundaries for cubic crystals under hydrostatic stress and uniaxial stress

Liu, Kai; Sluiter, Marcel H.F.

DOI
10.1016/j.mtla.2024.102071

Publication date
2024

Document Version
Final published version

Published in
Materialia

Citation (APA)
Liu, K., & Sluiter, M. H. F. (2024). Incompatibility stress at inclined grain boundaries for cubic crystals under hydrostatic stress and uniaxial stress. *Materialia*, *34*, Article 102071. https://doi.org/10.1016/j.mtla.2024.102071

Important note
To cite this publication, please use the final published version (if applicable).
Please check the document version above.

Copyright
Other than for strictly personal use, it is not permitted to download, forward or distribute the text or part of it, without the consent of the author(s) and/or copyright holder(s), unless the work is under an open content license such as Creative Commons.

Takedown policy
Please contact us and provide details if you believe this document breaches copyrights.
We will remove access to the work immediately and investigate your claim.

This work is downloaded from Delft University of Technology.
For technical reasons the number of authors shown on this cover page is limited to a maximum of 10.

MTLA 34 (2024) 102071

Contents lists available at ScienceDirect

Materialia

journal homepage: www.elsevier.com/locate/mtla

Full length article

Incompatibility stress at inclined grain boundaries for cubic crystals under hydrostatic stress and uniaxial stress

Kai Liu [a], Marcel H.F. Sluiter [a,b,*]

[a] Department of Materials Science and Engineering, Delft University of Technology, Mekelweg 2, Delft, 2628 CD, The Netherlands
[b] Department of Electromechanical, Systems and Metal Engineering, Ghent University (UGent), Technologiepark 903, Zwijnaarde (Ghent), B-9052, Belgium

ARTICLE INFO

MSC:
74A50

Keywords:
Grain boundary
Incompatibility stress
Anisotropy
Grain boundary inclination
Stress concentration

ABSTRACT

In a material under stress, grain boundaries may give rise to stress discontinuities. The stress state at grain boundaries strongly affects microscopic processes, such as diffusion and segregation, as well as failure initiation, such as fatigue, creep, and corrosion. Here the general condition of incompatibility stress at grain boundaries is studied with a bicrystal model for linear elastic materials. In materials with cubic crystal structures, it is proven that hydrostatic stress does not lead to a stress discontinuity at grain boundaries. For bicrystals with inclined grain boundaries under uniaxial stress, the extreme values of the incompatibility stress as a function of the inclination angle are obtained by a simulated annealing method. A simple criterion is proposed to classify cubic materials into three groups. For cubic crystals with at most moderate anisotropy, the highest incompatibility stress occurs when the grain boundary plane is perpendicular to the uniaxial stress. For highly anisotropic materials, such as alkali metals and polymorphic high-temperature phases, the highest incompatibility stress occurs on grain boundaries with an inclination of about 47°.

1. Introduction

Most commercial metals are polycrystalline with properties that are strongly dependent on the amount and character of grain boundaries (GBs). Due to the anisotropy of the elastic tensor and the discontinuity of crystal orientations across GBs, maintaining deformation compatibility causes the stress states near GBs to deviate significantly from the average stress state.

Many microscopic processes in materials are strongly influenced by stress states near GBs, such as diffusion [1–3], segregation [4–6], and (nano)void formation [7]. Therefore failure processes also are connected with the stress state at GBs, such as fatigue [8–12], creep [13–15] and stress corrosion cracking [16–19]. The initiation of phase transformation is also strongly influenced by the local stressstate [20–22].

The study of the stress state at GBs and its relation to GB parameters has been a challenge due to the many degrees of freedom of GBs [23]. Analytical solutions for the stress state near GBs were derived for several special grain boundaries [24,25]. For general grain boundaries, Richeton and Berbenni [26] proposed an analytical solution with a bicrystal model. The model was verified by comparing it with finite element method (FEM) simulations. The results were used to study the activation of slip systems near the $\Sigma 3\langle 111\rangle$ twin boundary [27]. Recently, Shawish and Mede [28] introduced a semi-analytical solution for the distribution of stresses along the GB normal within polycrystals under an arbitrary load with a perturbation method. Previously the current authors investigated the stresses near grain boundaries for applied loads perpendicular to the grain boundaries [29]. The GBs with the largest incompatibility stress were determined for all cubic materials with the GB plane being perpendicular to the external stress.

FEM provides a helpful tool for studying the stresses near GBs. By performing FEM simulation for the stress distribution in polycrystals under load, the relationship between stress states and GB parameters (grain orientation, GB inclination angle, etc.) is clarified by statistical methods [30,31] and machine learning [32]. These works revealed that the GB area, GB inclination angle, and the orientations of adjacent grains influence the occurrence of stress concentrations near GBs. However, these statistics-based correlations are descriptive rather than quantitative. In order to gain insight into the magnitude of stress discontinuities at an arbitrarily inclined GB in a general material and therefore take advantage of the local stress state, it is necessary to establish quantitative and physically meaningful rules between the GB characters, external stresses, and the stress discontinuities.

This work investigates the incompatibility stress for general GBs in materials with a cubic crystal structure with a bicrystal model. Section 2 introduces the bicrystal model for calculating the incompatibility

* Corresponding author at: Department of Materials Science and Engineering, Delft University of Technology, Mekelweg 2, Delft, 2628 CD, The Netherlands.
E-mail addresses: k.liu-3@tudelft.nl (K. Liu), m.h.f.sluiter@tudelft.nl (M.H.F. Sluiter).

https://doi.org/10.1016/j.mtla.2024.102071
Received 8 December 2023; Accepted 22 March 2024
Available online 23 March 2024
2589-1529/© 2024 The Author(s). Published by Elsevier B.V. on behalf of Acta Materialia Inc. This is an open access article under the CC BY license (http://creativecommons.org/licenses/by/4.0/).

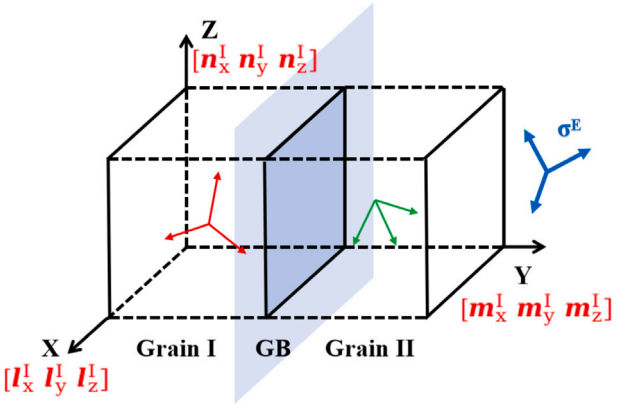

Fig. 1. (Color online) Schematic figure of the bicrystal model. Grains I (II) on the left (right side) are separated by a GB perpendicular to the global Y-axis. The GB is infinitely extended in the X and Z directions. The orientation of each grain is represented by three vectors represented by Miller indices. The label of the grain is shown with a superscript. The external stress σ^E can be of any type.

stress with a fixed GB plane under arbitrary external stress. An approximation for incompatibility stress for cubic materials under arbitrary external stress is derived in Section 3.1. In Section 3.2, we prove that hydrostatic external stress does not lead to any stress discontinuity at GBs. In Section 3.3, the incompatibility stress at inclined GBs is considered using a coordinate transformation. The extreme incompatibility stresses for GBs with various inclination angles are explored with a simulated annealing method. The influence of GB inclination angle on the magnitude of incompatibility stress is systematically explored.

2. Model description

We first consider the incompatibility stress for a GB fixed parallel to the XOZ plane under an arbitrary external stress σ^E. A schematic figure of the bicrystal model is shown as Fig. 1. The 3-dimensional space is divided into two semi-infinite half-spaces separated by the GB. The left (right) of the GB is grain I(II). The two grains consist of the same material.

The orientations of crystals can be conveniently described with Miller indices. For grain I,

$$\hat{e}^I = \begin{bmatrix} l_x^I & l_y^I & l_z^I \\ m_x^I & m_y^I & m_z^I \\ n_x^I & n_y^I & n_z^I \end{bmatrix}, \tag{1}$$

where $\boldsymbol{l}^I$, $\boldsymbol{m}^I$, $\boldsymbol{n}^I$ are normalized Miller indices of the crystallographic orientation of grain I corresponding to X, Y, and Z-axis in the global coordinate system, respectively, and analogously for grain II.

Within the continuum description of GBs, the following constraints apply to the bicrystal model.

1. The two grains are rigidly glued together at the GB. No relative motion is allowed at the GB.
2. The model contains only one infinitely extended GB. The interaction between GBs is not included.
3. There is a linear relation between stress and strain.

With Voigt notation (xx → 1, yy → 2, zz → 3, yz → 4, xz → 5, xy → 6) with the engineering convention ($\varepsilon_4 = 2\varepsilon_{xy}$), the constitutive equation of linear elastic material is

$$\begin{bmatrix} \epsilon_1 \\ \epsilon_2 \\ \epsilon_3 \\ \epsilon_4 \\ \epsilon_5 \\ \epsilon_6 \end{bmatrix} = \begin{bmatrix} s_{11} & s_{12} & s_{13} & s_{14} & s_{15} & s_{16} \\ s_{12} & s_{22} & s_{23} & s_{24} & s_{25} & s_{26} \\ s_{13} & s_{23} & s_{33} & s_{34} & s_{35} & s_{36} \\ s_{14} & s_{24} & s_{34} & s_{44} & s_{45} & s_{46} \\ s_{15} & s_{25} & s_{35} & s_{45} & s_{55} & s_{56} \\ s_{16} & s_{26} & s_{36} & s_{46} & s_{56} & s_{66} \end{bmatrix} \begin{bmatrix} \sigma_1 \\ \sigma_2 \\ \sigma_3 \\ \sigma_4 \\ \sigma_5 \\ \sigma_6 \end{bmatrix} \tag{2}$$

Since there is no constraint on the shape of the compliance matrix, the model is valid for all crystal structures.

The discontinuity of a scalar field $g(x_i)$ at the GB is denoted as

$$[[g]] = g^I - g^{II}. \tag{3}$$

According to the first constraint listed above, strain components in the GB plane are continuous,

$$[[\varepsilon_i]] = 0, \quad i,j = 1,3,5. \tag{4}$$

Since σ^E is a far-field stress, global stress equilibrium requires

$$\frac{1}{V}\int_V \sigma_i dV = \sigma_i^E, \tag{5}$$

where σ^E is the applied external stress [26]. Since the model assumes that each grain occupies half the space,

$$\sigma_i^E = \frac{1}{2}(\sigma_i^I + \sigma_i^{II}). \tag{6}$$

The tractions on the GB must be continuous, and the difference at the GB must vanish (Eq. (3)),

$$[[\sigma_i]] = 0, \quad i = 2,4,6. \tag{7}$$

σ^I and σ^{II} as function of σ^E for any GB can be calculated by solving Eqs. (2), (4), (6), and (7).

Eq. (7) shows that only in-plane components of incompatibility stress are non-zero. Then the stress states on both sides of the GB can be written as the superposition of σ^E and the additional stress field,

$$\begin{cases} \sigma^I = [\Delta\sigma_1 + \sigma_1^E, \sigma_2^E, \Delta\sigma_3 + \sigma_3^E, \sigma_4^E, \Delta\sigma_5 + \sigma_5^E, \sigma_6^E] \\ \sigma^{II} = [-\Delta\sigma_1 + \sigma_1^E, \sigma_2^E, -\Delta\sigma_3 + \sigma_3^E, \sigma_4^E, -\Delta\sigma_5 + \sigma_5^E, \sigma_6^E]. \end{cases} \tag{8}$$

The magnitudes of the three additional stress components, i.e. $\Delta\sigma_1$, $\Delta\sigma_3$, and $\Delta\sigma_5$, are influenced by the choice of the observation coordinate system. As is evident from the Mohr circle construction, $\Delta\sigma_5$ can be made to vanish by an appropriate rotation of the coordinate system while $\Delta\sigma_1$ and $\Delta\sigma_3$ cannot. In keeping consistency with previous work [29], the incompatibility stress (IS) is defined as

$$IS = \Delta\sigma_1 + \Delta\sigma_3. \tag{9}$$

The advantage of the definition is that IS is directly connected with hydrostatic stress σ_h at both sides of GBs, which is independent of the reference coordinate system,

$$\begin{aligned} [[\sigma_h]] &= \frac{2(\Delta\sigma_1 + \Delta\sigma_3)}{3} \\ &= \frac{2}{3} IS. \end{aligned} \tag{10}$$

The problem is in the elastic limit, therefore IS induced by each stress component σ_i^E is linearly proportional to the magnitude of σ_i^E. For a uniaxial σ^E, which is common in applications, it is convenient to define incompatibility factor IF as

$$IF = \frac{IS}{\sigma^E}. \tag{11}$$

3. Results and discussion

3.1. Approximation for incompatibility stress under arbitrary external stress for cubic crystals

The analytical solution shown in Section 2 is accurate but not intuitive. Here, an approximation for the incompatibility stress under arbitrary external stress is derived for cubic crystals.

In previous work [29], the compliance tensor after rotation (see Appendix) is shown. The compliance tensor before ($\boldsymbol{S}$, with Voigt notation) and after rotation ($\boldsymbol{S}'$) can be written as

$$\boldsymbol{S}' = \boldsymbol{S} + \chi \boldsymbol{F}(\boldsymbol{l},\boldsymbol{m},\boldsymbol{n}) \tag{12}$$

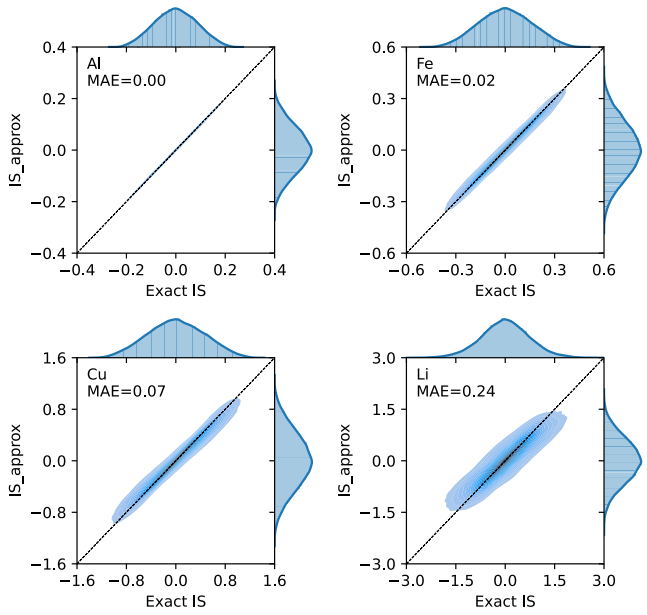

Fig. 2. Comparison between incompatibility stress calculated exactly with Eq. (9) and estimated with Eq. (17) for Al, Fe(BCC), Cu, and Li (in the sequence of ascending anisotropy). The distribution of IS obtained exactly and approximately (Eq. (17)) are presented in histograms at the top and right side of each scatter plot, respectively. Dashed lines are guides to the eye.

in which $\boldsymbol{l}$, $\boldsymbol{m}$, and $\boldsymbol{n}$ describe the rotation (see Eq. (1)), F is a 6 by 6 matrix defined in Ref. [29], while χ gives the anisotropy in the compliance of the material,

$$\chi = 2s_{11} - 2s_{12} - s_{44}. \tag{13}$$

Under σ_2^{E} [29],

$$IS \approx \frac{2[[F_{22}]]\sigma_2^{\mathrm{E}}\chi}{(F_{22}^{\mathrm{I}} + F_{22}^{\mathrm{II}})\chi + 4s_{11} + 4s_{12}}, \tag{14}$$

with

$$F_{22} = -(m_{\mathrm{x}}^2 m_{\mathrm{y}}^2 + m_{\mathrm{x}}^2 m_{\mathrm{z}}^2 + m_{\mathrm{y}}^2 m_{\mathrm{z}}^2). \tag{15}$$

As our description is in the linear elastic limit, the superposition principle applies to IS, which means IS induced by each component of σ^E can be treated separately. With similar simplification, IS for arbitrary σ^E is estimated with superposition principle, as

$$IS_{approx} = \frac{2\sum_{i=1}^{6}[[F_{i2}]]\sigma_i^{\mathrm{E}}\chi}{(F_{22}^{\mathrm{I}} + F_{22}^{\mathrm{II}})\chi + 4s_{11} + 4s_{12}} \tag{16}$$

Noticing $(F_{22}^{\mathrm{I}} + F_{22}^{\mathrm{II}})$ approaches to $-\frac{1}{3}$ for configurations with high IS, Eq. (16) is further simplified as

$$IS_{approx} = \frac{6\chi}{10s_{11} + 14s_{12} + s_{44}} \sum_{i=1}^{6}[[F_{i2}]]\sigma_i^{\mathrm{E}} \tag{17}$$

The accuracy of Eq. (17) is illustrated in Fig. 2. For Al, Fe(BCC), Cu, and Li (in order of increasing elastic anisotropy), the IS obtained by Eq. (17) for 50 000 arbitrarily oriented bicrystals under randomly chosen external stress states (each of the six stress components is randomly chosen in $[-1, 1]$) are compared with exact solutions to Eq. (9). The histograms at the top and right side of each scatter plot show the distributions of IS by analytical solution and by approximation, respectively. The mean absolute error (MAE) for each metal is shown in the figure.

For Al, Fe(BCC), and Cu, the IS obtained by approximation (Eq. (17)) are in good agreement with the analytical results. For Li, the approximation underestimates the extreme value of IS. The extraordinarily high level of IS in materials with high anisotropy is further discussed in Section 3.3.

Eq. (17) shows that the value of IS is controlled by three factors, i.e. the material elastic property (χ and compliance components), the difference of the orientations of the two grains ($[[F_{i2}]]$), and σ^{E}. That means that for a given σ^{E}, the configurations of the bicrystal that lead to extreme IS are the same for all cubic materials. Such is the case for uniaxial stress perpendicular to the GB where it could be proven that the $\langle 100\rangle\langle 111\rangle$ GB gives the largest IS for all cubic materials [29]. Conversely, one can also seek to determine which σ^{E} leads to the largest IS for a bicrystal with given orientations of the two grains using Eq. (17). Particularly for polycrystals with strong textures, for which anisotropic mechanical properties are well documented [33,34], it is promising to identify the relation between loading conditions and the distribution of IS at GBs.

3.2. Incompatibility stress in cubic crystals under hydrostatic external stress for bicrystal model

Here we prove hydrostatic external stress does not lead to incompatibility stress at the GB in the bicrystal model. The absence of hydrostatically induced incompatibility stresses in cubic materials can be intuitively derived from a *Gedankenexperiment*: Hydrostatically compressing a monocrystalline sphere with a cubic crystal structure causes a volume change only, without change of shape, irrespective of the grain's orientation. When two spheres with different orientations are cut in half and subsequently recombined to create a bicrystal sphere, no additional stress is necessary as the cut sections match perfectly. Consequently, hydrostatic stress does not induce IS in cubic crystals. It follows that in cubic crystals the deviatoric stress only causes IS. However, in lower symmetry crystal structures, e.g. hexagonal, hydrostatic external stress generally contributes to IS at GBs. A detailed proof is shown in Appendix.

Since the stress state at GBs under hydrostatic stress can hardly be experimentally determined, there is no direct evidence for the findings. The molecular dynamics simulation of the segregation energy for several alloy systems by Zhang et al. [35] indirectly confirms our findings. In the simulation, hydrostatic stresses with the magnitude of 2 to 12 GPa were applied to polycrystal models, and the distributions of segregation energy were studied. The local atomic stress analysis showed that for Al-Mg, Al-Ni, and Ni-Nb alloys, the external hydrostatic stress level led to minor changes to the fraction of GB sites that were under a tensile stress state. Noticing the matrices of the alloys are all cubic crystals, the simulations match the analytical conclusion well.

3.3. Bicrystal model with inclined grain boundary under uniaxial external stress for cubic crystals

Assume the uniaxial external stress is along the global Y-axis, i.e. $\sigma^{\mathrm{E}} = [0, 1, 0, 0, 0, 0]$, the schematic figure for the bicrystal model with inclined GB is shown as Fig. 3. The two grains are semi-infinite and the model is still subject to the constraints described in Section 2. The orientation of the grain boundary is defined with θ, the angle between the GB normal n and the global Y-axis, and ϕ, the angle between the projection of $\vec{n}$ on XOZ plane and X-axis. Experimentally, the distribution of θ for GBs in polycrystals can be measured, as one of the five parameters of GBs [23]. In Section 2, IS for a GB parallel to the XOZ plane under an arbitrary σ^{E} is derived. By defining a GB coordinate system in which the GB aligns to the local XOZ plane and representing the problem within the GB coordinate system, the stress state for an inclined GB can be solved with the same method.

The normal vector of GB plane $\vec{n}$ is uniquely represented as $[sin\theta cos\phi \;\; cos\theta \;\; -sin\theta sin\phi]$. Since there is no constraint on the choice of

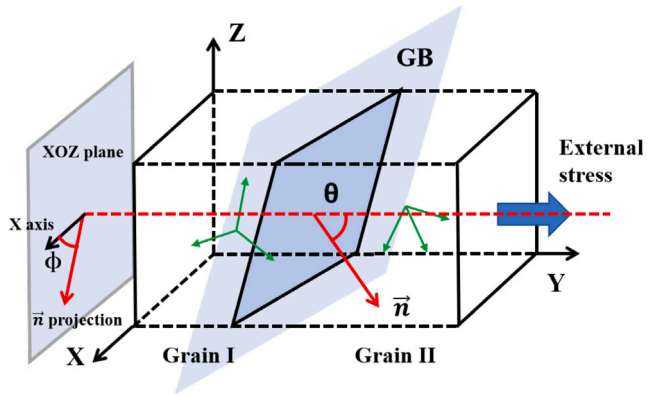

Fig. 3. The schematic figure of the bicrystal model with inclined grain boundary under uniaxial external stress. The orientation of the grain boundary is defined with θ, the angle between the grain boundary normal $\vec{n}$ and the global Y-axis, and ϕ, the angle between the projection of $\vec{n}$ on the XOZ plane and X-axis.

the other two basis vectors, for convenience, the GB coordinate system can be chosen as

$$Q = \begin{bmatrix} sin\phi & 0 & cos\phi \\ sin\theta cos\phi & cos\theta & -sin\theta sin\phi \\ -cos\theta cos\phi & sin\theta & cos\theta sin\phi \end{bmatrix}. \tag{18}$$

For a grain with orientation $\hat{e}$ defined in global coordinate system, the corresponding orientation $\hat{e}^{GB}$ in the GB coordinate system Q can be obtained by

$$\hat{e}^{GB} = Q\hat{e}. \tag{19}$$

For uniaxial external stress with a magnitude of σ^E along the global Y axis, the external stress acting on the GB plane $\sigma^{E,GB}$ is calculated as

$$\sigma^{E,GB} = Q \cdot \begin{bmatrix} 0 & 0 & 0 \\ 0 & \sigma^E & 0 \\ 0 & 0 & 0 \end{bmatrix} \cdot Q^T = \sigma^E \begin{bmatrix} 0 & 0 & 0 \\ 0 & cos^2\theta & sin\theta cos\theta \\ 0 & sin\theta cos\theta & sin^2\theta \end{bmatrix}. \tag{20}$$

From Eq. (20), $\sigma^{E,GB}$ is only controlled by θ, which ranges from 0 (GB perpendicular to the uniaxial external stress) to 90° (GB parallel to the uniaxial external stress). The second degree of freedom of the GB plane, ϕ, is included in the coordinate transformation of elastic tensors for the two grains (Eq. (19)). IF_θ^{max} denotes the maximum IF over ϕ values for GBs with a specific inclination angle θ while IF_{max}^{max}, IF_{min}^{max} denotes the maximum and minimum IF for bicrystals for all θ values, respectively.

In our previous work [29], GBs perpendicular to the uniaxial external stress ($\theta = 0°$) have been studied systematically. $IF_{\theta=0°}^{max}$, the maximum incompatibility factor for GB with $\theta = 0°$, was found as a function of elastic components,

$$\begin{aligned} IF_{\theta=0°}^{max} &= \frac{4s_{11} - 4s_{12} - 2s_{44}}{10s_{11} + 14s_{12} + s_{44}} \\ &= \frac{-2(C_{11} - C_{12} - 2C_{44}(C_{11} + 2C_{12}))}{(10C_{11} - 4C_{12})C_{44} + (C_{11} - C_{12})(C_{11} + 2C_{12})}. \end{aligned} \tag{21}$$

For several materials Eq. (21) yields negative $IF_{\theta=0°}^{max}$. Since IF for a given bicrystal changes its sign when the two grains exchange the label, we use the absolute value to assess the magnitude of $IF_{\theta=0°}^{max}$. For bicrystal with GB plane inclined by arbitrary θ, no analytical solution for IF_θ^{max} was found. For θ ranging from 0 to 90° with 1° increments, a simulated annealing approach was applied to search for the extreme value of IF for each θ. For several materials in cubic crystal (including metals, intermetallics, oxides, and carbides), the elastic components, Zener ratio ($A = \frac{2C_{44}}{C_{11}-C_{12}}$), $IF_{\theta=0°}^{max}$, the θ corresponding to IF_{max}^{max} and IF_{min}^{max} are listed in Table 1, in a sequence of ascending $|IF_{\theta=0°}^{max}|$.

To emphasize the influence of θ and to make various materials comparable, IF_θ^{max} is normalized by $|IF_{\theta=0°}^{max}|$. Normalized IF_θ^{max} curves are shown as function of θ in Fig. 4.

Table 1 and Fig. 4 clearly illustrate that cubic materials can be classified into three groups. Materials in each group have similar features of the distribution of IF_θ^{max}. The criteria and features of each group are listed as follows.

1. For materials with $|IF_{\theta=0°}^{max}| < 0.7$, including metals, carbides, and oxides, IF_θ^{max} decreases when θ increases, IF_θ^{max} achieves its maximum when $\theta = 0°$, while achieves its minimum at $\theta = 90°$, as is shown in Fig. 4(a). The influence of θ on IF_θ^{max} is getting smaller with the increase of $IF_{\theta=0°}^{max}$, which is contrary to intuition. For example, the relative variation of IF_θ^{max} for iron (BCC) is about 13% while the value for aluminum is 22%. In this group, the $IF_{\theta=0°}^{max}$ for some materials are negative. These materials have slightly higher $IF_{\theta=90°}^{max}$, comparing with materials with positive $IF_{\theta=0°}^{max}$ of same magnitude.
2. For materials with medium anisotropy, i.e. $0.7 \le |IF_{\theta=0°}^{max}| < 1.0$, including Group 11 elements and Pd, IF_θ^{max} have small relative variation (about 10%) with respect to θ. IF_{max}^{max} is achieved for GB with about 32°, and IF_{min}^{max} is at $\theta = 90°$, as is shown in Fig. 4(b).
3. For materials with high anisotropy, i.e. $IF_{\theta=0°}^{max} > 1.0$, including lead, alkali metals, and polymorphic high-temperature stable phases for several metals, IF_θ^{max} significantly rises when θ rises from 0° to about 45°, as is shown in Fig. 4(c). IF^{max} is achieved when θ is $43° - 47°$. For these materials, the difference of IF_θ^{max} with the variation of θ is amplified by their high $IF_{\theta=0°}^{max}$.

Also, we notice $|IF_{\theta=0°}^{max}|$ is a good indicator for the classification of materials, compared with the Zener ratio. For given elastic components, $|IF_{\theta=0°}^{max}|$ calculated from Eq. (21) can properly predicts the shape of IF_θ^{max}, as well as the approximate range for IF_θ^{max}, as is shown in Fig. 4(d).

The configurations of the bicrystal (i.e. the orientations of the two grains and the GB plane) in the global coordinate system corresponding to IF_θ^{max} are also of concern. For θ less than 10°, the problem is similar to bicrystals with GB fixed perpendicular to the uniaxial σ^E. It is found that IF for GBs which have two grains with crystallographic orientation of $\langle 100 \rangle$ and $\langle 111 \rangle$ along the direction of σ^E in the global coordinate system, respectively, are close to IF_θ^{max}. Configurations that correspond to IF_{max}^{max} and IF_{min}^{max} are obtained with a simulated annealing method, as is listed in Table 2. Since exact θ and configurations for IF^{max} are not the same for materials with medium to high anisotropy, the configurations given in the list are good approximations of the exact orientations.

For two grains with orientations given in Table 2, keep θ varying from 0° to 90° and $\phi = 0°$, IF for three typical metals are shown in Fig. 5. It can be observed that even for a bicrystal system with only one degree of freedom (i.e. θ), IF could vary in a wide range. Curves shown in Fig. 4 are the upper envelopes of IF curves for all possible configurations of the bicrystal with different material properties.

Song et al. [49] studied the relation between intergranular stress concentration and GB orientations in Ni-based superalloy statistically by microscopic characterizations, and found that GB inclination angle has little influence on the stress concentration tendency. The necessity of two degrees of freedom for GB orientation in the determination of IF explains why the microscopic characterization (which generally shows cut lines of GB planes) failed to reveal the influence of GB orientation on stress concentration.

The value of IS indicates stress discontinuity and stress concentration, as described in Eq. (10). A direct application of the hydrostatic stress at GBs is the segregation tendency. Both Monte Carlo simulation [50] and crystal plasticity FEM [51] confirmed the profound influence of local hydrostatic stress on the segregation tendency. Jothi

Table 1
Elastic components (C_{11}, C_{12}, and C_{44}), anisotropy indicator (Zener ratio A and $IF^{\max}_{\theta=0^\circ}$), the range of $IF^{\max}_{\theta}$ and the grain boundary inclination angle θ corresponding to the maximum and minimum of $IF^{\max}_{\theta}$ for common cubic materials. The materials are listed in a sequence of ascending elastic anisotropy and divided into three groups according to the magnitude of their $IF^{\max}_{\theta}$.

Material	C_{11}	C_{12}	C_{44}	A	$IF^{\max}_{\theta=0^\circ}$	Range of $IF^{\max}_{\theta}$	θ for $IF^{\max}_{\max}$	θ for $IF^{\max}_{\min}$
Unit	GPa	GPa	GPa	Dimensionless			Degree	
W [36]	523.0	203.0	160.0	1.00	0.0	0.0	–	–
TiC [37]	500.0	113.0	175.0	0.90	−0.0499	[0.0381, 0.0499]		
Fe_3O_4 [38]	275.0	104.0	95.5	1.12	0.0632	[0.0482, 0.0632]		
ZrC [39]	472.0	98.7	159.3	0.85	−0.0780	[0.0603, 0.0780]		
Al [36]	108.0	62.0	28.3	1.23	0.1437	[0.1118, 0.1437]		
Cr [36]	348.0	67.0	100.0	0.71	−0.1710	[0.1367, 0.1710]		
V [36]	230.0	120.0	43.1	0.78	−0.1719	[0.1359, 0.1719]		
Mo [36]	465.0	163.0	109.0	0.72	−0.1970	[0.1578, 0.1970]		
Si [36]	165.0	63.0	79.1	1.55	0.2332	[0.1857, 0.2332]	0	90
Ir [36]	600.0	260.0	270.0	1.59	0.2605	[0.2090, 0.2605]		
Ta [36]	264.0	158.0	82.6	1.56	0.3013	[0.2444, 0.3013]		
GaAs [40]	118.8	53.7	59.4	1.82	0.3349	[0.2742, 0.3349]		
Pt [41]	347.0	251.0	76.5	1.59	0.3583	[0.2951, 0.3583]		
$MgAl_2O_4$ [42]	298.6	153.7	157.6	2.18	0.4472	[0.3777, 0.4472]		
Nb [36]	245.0	132.0	28.4	0.50	−0.5104	[0.4471, 0.5104]		
Fe(BCC) [36]	230.0	135.0	117.0	2.46	0.5485	[0.4767, 0.5485]		
Ni [36]	247.0	153.0	122.0	2.60	0.5954	[0.5246, 0.5954]		
Pd [36]	221.0	171.0	70.8	2.83	0.7573	[0.7007, 0.7639]	30	
Cu [36]	169.0	122.0	75.3	3.20	0.7785	[0.7247, 0.7888]	32	90
Ag [36]	122.0	92.0	45.5	3.03	0.7786	[0.7251, 0.7887]	32	
Au [36]	191.0	162.0	42.2	2.91	0.8368	[0.7936, 0.8588]	36	
Pb [36]	48.8	41.4	14.8	4.00	1.0170	[1.0170, 1.1033]	43	
NiTi(B2) [43]	175.0	153.0	48.0	4.36	1.0917	[1.0917, 1.2191]	45	
Ti(BCC) [44]	97.7	82.7	37.5	5.00	1.1204	[1.1204, 1.2686]	46	
Fe(FCC) [45]	188.0	156.0	87.0	5.44	1.1335	[1.1335, 1.2926]	46	0
Na [36]	7.6	6.3	4.3	6.62	1.2052	[1.2052, 1.4242]	47	
K [46]	3.7	3.2	1.9	7.60	1.3063	[1.3063, 1.6303]	47	
Zr(BCC) [47]	104.0	93.0	38.0	6.91	1.3194	[1.3194, 1.6548]	47	
Li [48]	13.4	11.3	9.6	9.14	1.3266	[1.3266, 1.6816]	47	

Table 2
The orientations for the bicrystal with varying anisotropy to achieve $IF^{\max}_{\max}$ and $IF^{\max}_{\min}$. $\boldsymbol{l}$ and $\boldsymbol{m}$ are the Miller indices along the global X- and Y-axis, respectively. θ, the inclination angle of the grain boundary plane, is given in Table 1. ϕ, the second degree of freedom of the grain boundary plane, is fixed as 0° for all the configurations.

Anisotropy	Orientations for $IF^{\max}_{\max}$		Orientations for $IF^{\max}_{\min}$	
	Grain I	Grain II	Grain I	Grain II
$-0.7 < IF^{\max}_{\theta=0^\circ} < 0$	$\boldsymbol{m}^{\mathrm{I}} = \frac{1}{\sqrt{3}}\langle 1\ \ 1\ \ 1\rangle$	$\boldsymbol{m}^{\mathrm{II}} = \langle 1\ \ 0\ \ 0\rangle$	$\boldsymbol{l}^{\mathrm{I}} = [0\ \ 1\ \ 0]$ $\boldsymbol{m}^{\mathrm{I}} = \frac{1}{\sqrt{2}}[1\ \ 0\ \ 1]$	$\boldsymbol{l}^{\mathrm{II}} = \frac{1}{\sqrt{2}}[1\ \ 0\ \ -1]$ $\boldsymbol{m}^{\mathrm{II}} = \frac{1}{\sqrt{2}}[1\ \ 0\ \ 1]$
$0 < IF^{\max}_{\theta=0^\circ} < 0.7$				
$0.7 \le IF^{\max}_{\theta=0^\circ} < 1.0$	$\boldsymbol{l}^{\mathrm{I}} = \frac{1}{\sqrt{37}}[6\ \ 0\ \ -1]$ $\boldsymbol{m}^{\mathrm{I}} = \frac{1}{\sqrt{37}}[-1\ \ 0\ \ -6]$	$\boldsymbol{l}^{\mathrm{II}} = \frac{1}{\sqrt{14}}[\sqrt{5}\ \ \sqrt{5}\ \ 2]$ $\boldsymbol{m}^{\mathrm{II}} = \frac{1}{\sqrt{7}}[1\ \ 1\ \ -\sqrt{5}]$	$\boldsymbol{l}^{\mathrm{I}} = \frac{1}{\sqrt{2}}[1\ \ 0\ \ 1]$ $\boldsymbol{m}^{\mathrm{I}} = \frac{1}{\sqrt{2}}[1\ \ 0\ \ -1]$	$\boldsymbol{l}^{\mathrm{II}} = \frac{1}{\sqrt{2}}[1\ \ 0\ \ 1]$ $\boldsymbol{m}^{\mathrm{II}} = [0\ \ 1\ \ 0]$
$IF^{\max}_{\theta=0^\circ} \ge 1.0$	$\boldsymbol{l}^{\mathrm{I}} = \frac{1}{\sqrt{26}}[5\ \ 1\ \ 0]$ $\boldsymbol{m}^{\mathrm{I}} = \frac{1}{\sqrt{26}}[-1\ \ 5\ \ 0]$	$\boldsymbol{l}^{\mathrm{II}} = \frac{1}{\sqrt{54}}[-5\ \ 5\ \ -2]$ $\boldsymbol{m}^{\mathrm{II}} = \frac{1}{\sqrt{27}}[-1\ \ 1\ \ 5]$	$\boldsymbol{m}^{\mathrm{I}} = \frac{1}{\sqrt{3}}\langle 1\ \ 1\ \ 1\rangle$	$\boldsymbol{m}^{\mathrm{II}} = \langle 1\ \ 0\ \ 0\rangle$

et al. [52] studied the hydrogen re-distribution near ⟨001⟩ tilt GBs induced by the incompatibility stress with the aim to identify GBs with low hydrogen concentration tendency in nickel. In this work, a wide range of GB configurations and stresses were analyzed to relate the relative magnitude of IF to the inclination of GBs. The value of $IF^{\max}_{\theta}$ and its variation with respect to θ for cubic crystals presented here can provide insights for segregation engineering [53].

4. Conclusion

This work examines the difference of stress states on both sides of GBs under arbitrary external stress in linear elastic cubic materials with a bicrystal model. For linear elasticity, there is a proportionality between the additional normal stress at GBs and the applied uniaxial stress. We define the ratio of the additional normal stress at GBs over the applied uniaxial stress as the incompatibility factor(IF). The variation of $IF^{\max}_{\theta}$, the highest IF for a GB with an inclination angle θ and two grains with arbitrary orientations, is explored systematically. The following conclusions are obtained:

1. The incompatibility stress for GB under external applied stress σ^{E} can be estimated with
$$IS_{approx} = \frac{6\chi}{10s_{11} + 14s_{12} + s_{44}} \sum_{i=1}^{6} [[F_{i2}]]\sigma_i^{\mathrm{E}}, \tag{22}$$
where s_{11}, s_{12}, s_{44}, and $\chi = 2s_{11} - 2s_{12} - s_{44}$ show the influence of the material elastic property while the $[[F_{i2}]]$ show the influence of the orientations of the two grains.
2. For cubic crystals, hydrostatic external stress does not induce any incompatibility stress at GBs. The incompatibility stress is caused by the deviatoric stress only.
3. The anisotropy of cubic materials is evaluated with $IF^{\max}_{\theta=0^\circ}$, which is a simple function of s_{11}, s_{12}, and s_{44}. $IF^{\max}_{\theta=0^\circ}$ is somewhat correlated with the Zener anisotropy A or the universal elastic anisotropy index [54]. Cubic materials are classified into

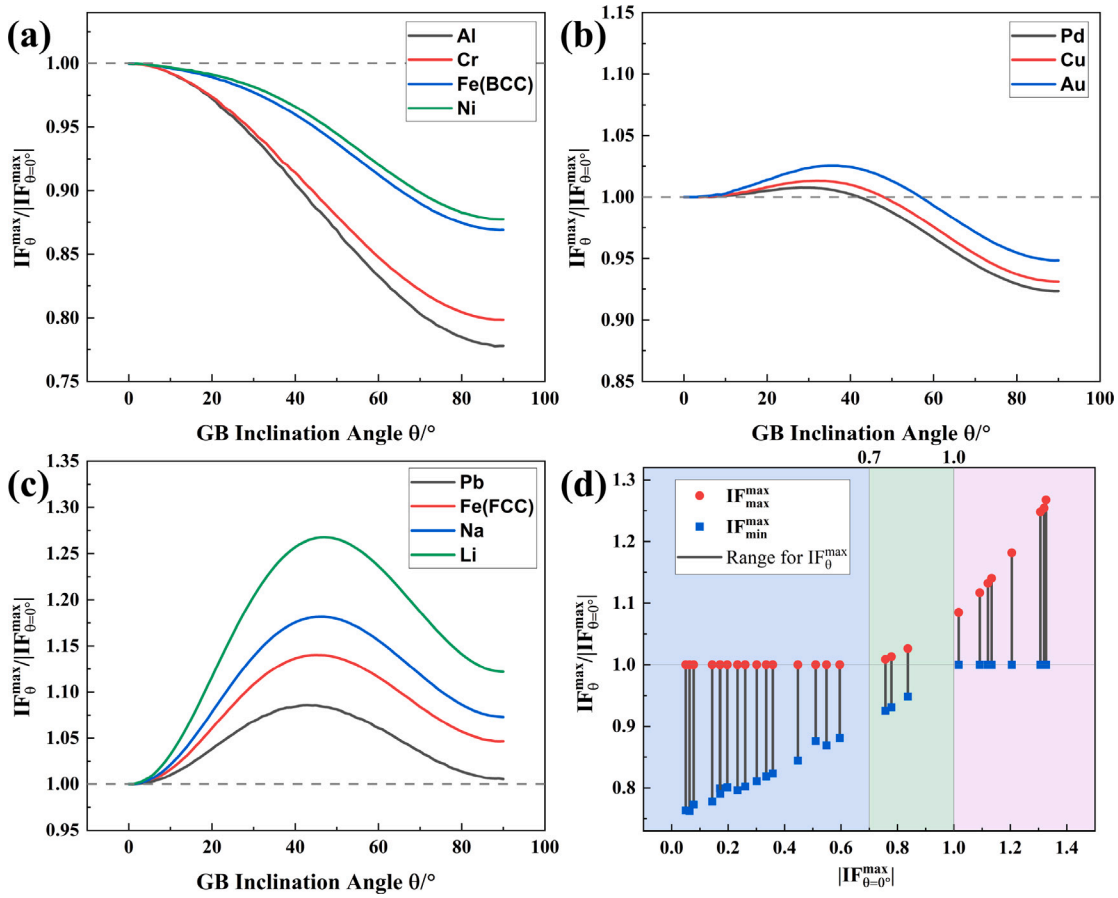

Fig. 4. The variation of the maximum incompatibility factor $IF_{\theta}^{\max}$ with respect to the grain boundary inclination angle θ for (a) materials with $|IF_{\theta=0^\circ}^{\max}| < 0.7$; (b) materials with $0.7 \leq |IF_{\theta=0^\circ}^{\max}| < 1.0$; (c) materials with $|IF_{\theta=0^\circ}^{\max}| > 1.0$. Figure (d) shows the range of normalized $IF_{\theta}^{\max}$ for all materials listed in Table 1. $IF_{\theta}^{\max}$ is scaled by $|IF_{\theta=0^\circ}^{\max}|$ (as is listed in Table 1) to emphasis the influence of θ.

three groups according to the magnitude of $IF_{\theta=0^\circ}^{\max}$. Materials within each group share that the most extreme incompatibility stress occurs for (1) the same grain boundary inclination angle with respect to the direction of the σ^{E}, (2) the same bicrystal grain orientations, and (3) display the same variation of the incompatibility stress with respect to the inclination angle.

4. Only materials with small $IF_{\theta=0^\circ}^{\max}$ values (and small Zener anisotropy A), exhibit the highest additional stress at GBs which are perpendicular to the uniaxial σ^{E}. More anisotropic cubic materials exhibit the highest additional stress at inclined GBs.
5. $IF_{\theta}^{\max}$ for materials with high anisotropy, such as alkali metals and polymorphic high-temperature phases [NiTi(B2), Fe(FCC), and Ti(BCC)], are the most affected by θ. These materials would have the highest additional stress at GBs with 47° inclination with respect to the uniaxial σ^{E}.

CRediT authorship contribution statement

Kai Liu: Conceptualization, Formal analysis, Investigation, Methodology, Software, Validation, Visualization, Writing – original draft, Writing – review & editing. **Marcel H.F. Sluiter:** Conceptualization, Investigation, Methodology, Supervision, Validation, Writing – review & editing.

Declaration of competing interest

The authors, declare that they have no known competing financial interests or personal relationships that could have appeared to influence the work reported in this paper.

Acknowledgments

The authors gratefully acknowledge financial support from the China Scholarship Council (CSC, No. 202006120016).

Appendix. Incompatibility stress under hydrostatic external stress

Ref. [29] showed that the compliance tensor after rotation ($\boldsymbol{S}'$, with Voigt notation) can be written as

$$S' = \begin{bmatrix} s_{11}+F_{11}\chi & s_{12}+F_{12}\chi & s_{12}+F_{13}\chi & F_{14}\chi & F_{15}\chi & F_{16}\chi \\ & s_{11}+F_{22}\chi & s_{12}+F_{23}\chi & F_{24}\chi & F_{25}\chi & F_{26}\chi \\ & & s_{11}+F_{33}\chi & F_{34}\chi & F_{35}\chi & F_{36}\chi \\ & & & s_{44}+F_{44}\chi & F_{45}\chi & F_{46}\chi \\ & symmetric & & & s_{44}+F_{55}\chi & F_{56}\chi \\ & & & & & s_{44}+F_{66}\chi \end{bmatrix} \tag{A.1}$$

where F_{ij} are polynomials of l, m, n, as

$$F_{11} = -(l_{\mathrm{x}}^2 l_{\mathrm{y}}^2 + l_{\mathrm{x}}^2 l_{\mathrm{z}}^2 + l_{\mathrm{y}}^2 l_{\mathrm{z}}^2) \tag{A.2}$$

$$F_{12} = -(m_{\mathrm{x}} m_{\mathrm{y}} l_{\mathrm{x}} l_{\mathrm{y}} + m_{\mathrm{x}} m_{\mathrm{z}} l_{\mathrm{x}} l_{\mathrm{z}} + m_{\mathrm{y}} m_{\mathrm{z}} l_{\mathrm{y}} l_{\mathrm{z}}) \tag{A.3}$$

$$F_{22} = -(m_{\mathrm{x}}^2 m_{\mathrm{y}}^2 + m_{\mathrm{x}}^2 m_{\mathrm{z}}^2 + m_{\mathrm{y}}^2 m_{\mathrm{z}}^2) \tag{A.4}$$

$$F_{13} = -(n_{\mathrm{x}} n_{\mathrm{y}} l_{\mathrm{x}} l_{\mathrm{y}} + n_{\mathrm{x}} n_{\mathrm{z}} l_{\mathrm{x}} l_{\mathrm{z}} + n_{\mathrm{y}} n_{\mathrm{z}} l_{\mathrm{y}} l_{\mathrm{z}}) \tag{A.5}$$

$$F_{23} = -(n_{\mathrm{x}} n_{\mathrm{y}} m_{\mathrm{x}} m_{\mathrm{y}} + n_{\mathrm{x}} n_{\mathrm{z}} m_{\mathrm{x}} m_{\mathrm{z}} + n_{\mathrm{y}} n_{\mathrm{z}} m_{\mathrm{y}} m_{\mathrm{z}}) \tag{A.6}$$

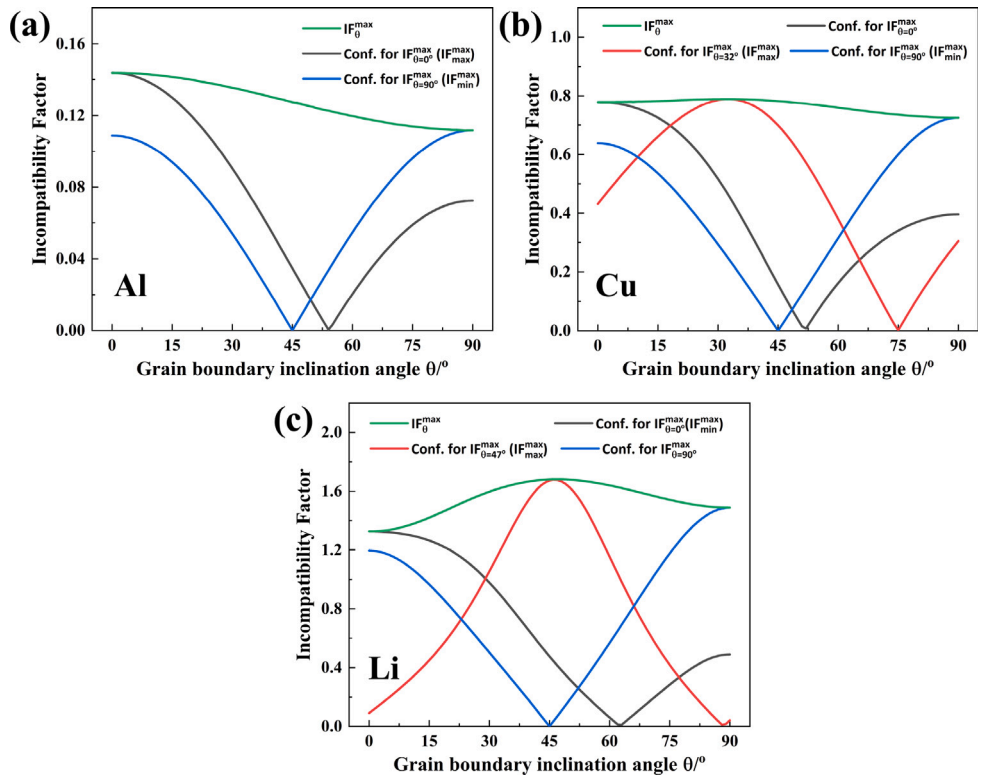

Fig. 5. The variation of IF as a function of the grain boundary inclination angle for special configurations ($IF^{\max}_{\max}$, $IF^{\max}_{\min}$, $IF^{\max}_{\theta=0^\circ}$, and $IF^{\max}_{\theta=90^\circ}$) for three typical material: (a) low-anisotropy material Al; (b) medium-anisotropy material Cu; and (c) high-anisotropy material Li. Curves for $IF^{\max}_{\theta}$, as the upper envelope of IF curves for all possible configurations of the bicrystal, are also presented.

$$F_{33} = -(n_x^2 n_y^2 + n_x^2 n_z^2 + n_y^2 n_z^2) \tag{A.7}$$

Under hydrostatic external stress, the strain for a rotated grain is

$$\varepsilon^H = \boldsymbol{S}' \begin{bmatrix} \sigma^H \\ \sigma^H \\ \sigma^H \\ 0 \\ 0 \\ 0 \end{bmatrix} = \sigma^H \begin{bmatrix} s_{11} + 2s_{12} + \chi(F_{11} + F_{12} + F_{13}) \\ s_{11} + 2s_{12} + \chi(F_{21} + F_{22} + F_{23}) \\ s_{11} + 2s_{12} + \chi(F_{31} + F_{32} + F_{33}) \\ 0 \\ 0 \\ 0 \end{bmatrix}. \tag{A.8}$$

Considering the orthonormality of $\boldsymbol{l}$, $\boldsymbol{m}$, and $\boldsymbol{n}$ of $\hat{\boldsymbol{e}}$,

$$\begin{aligned} F_{11} + F_{12} + F_{13} = &- [(l_x l_y + m_x m_y + n_x n_y) l_x l_y + \\ &(l_x l_z + m_x m_z + n_x n_z) l_x l_z + \\ &(l_y l_z + m_y m_z + n_y n_z) l_y l_z] \\ = &- (0 \cdot l_x l_y + 0 \cdot l_x l_z + 0 \cdot l_y l_z) \\ = &\ 0. \end{aligned} \tag{A.9}$$

Analogously it can be proven (see Supplement of Ref [29]. Eq.2-5) that

$$F_{i1} + F_{i2} + F_{i3} = 0, \quad i = 1, \ldots, 6. \tag{A.10}$$

Then the strain

$$\varepsilon^H = \sigma^H \begin{bmatrix} s_{11} + 2s_{12} \\ s_{11} + 2s_{12} \\ s_{11} + 2s_{12} \\ 0 \\ 0 \\ 0 \end{bmatrix} \tag{A.11}$$

for cubic crystals with arbitrary orientations and does not vary under rotation. Therefore there is no strain incompatibility between two crystals that are rotated relative to one another. Hence, there is no incompatibility stress either.

References

[1] N.E.B. Cowern, Diffusion in a single crystal within a stressed environment, Phys. Rev. Lett. 99 (15) (2007) 1–4, http://dx.doi.org/10.1103/PhysRevLett.99.155903.

[2] D.N. Ilin, N. Saintier, J.-M. Olive, R. Abgrall, I. Aubert, Simulation of hydrogen diffusion affected by stress-strain heterogeneity in polycrystalline stainless steel, Int. J. Hydrog. Energy 39 (5) (2014) 2418–2422, http://dx.doi.org/10.1016/j.ijhydene.2013.11.065.

[3] H. Abdolvand, Progressive modelling and experimentation of hydrogen diffusion and precipitation in anisotropic polycrystals, Int. J. Plast. 116 (2019) 39–61, http://dx.doi.org/10.1016/j.ijplas.2018.12.005.

[4] P. Lejček, S. Hofmann, Thermodynamics and structural aspects of grain boundary segregation, Crit. Rev. Solid State Mater. Sci. 20 (1) (1995) 1–85, http://dx.doi.org/10.1080/10408439508243544.

[5] X. Zhou, J. Song, Effect of local stress on hydrogen segregation at grain boundaries in metals, Mater. Lett. 196 (2017) 123–127, http://dx.doi.org/10.1016/j.matlet.2017.03.035.

[6] F. Fischer, G. Schmitz, S.M. Eich, A systematic study of grain boundary segregation and grain boundary formation energy using a new copper–nickel embedded-atom potential, Acta Mater. 176 (2019) 220–231, http://dx.doi.org/10.1016/j.actamat.2019.06.027.

[7] J. Chen, S.J. Fensin, Associating damage nucleation and distribution with grain boundary characteristics in Ta, Scr. Mater. 187 (2020) 329–334, http://dx.doi.org/10.1016/j.scriptamat.2020.06.035.

[8] N.J. Teng, T.H. Lin, Elastic anisotropy effect of crystals on polycrystal fatigue crack initiation, J. Eng. Mater. Technol. 117 (4) (1995) 470–477, http://dx.doi.org/10.1115/1.2804741.

[9] H. Vehoff, A. Nykyforchyn, R. Metz, Fatigue crack nucleation at interfaces, Mater. Sci. Eng. A 387–389 (1-2 SPEC. ISS.) (2004) 546–551, http://dx.doi.org/10.1016/j.msea.2003.12.094.

[10] M.D. Sangid, H.J. Maier, H. Sehitoglu, The role of grain boundaries on fatigue crack initiation - An energy approach, Int. J. Plast. 27 (5) (2011) 801–821, http://dx.doi.org/10.1016/j.ijplas.2010.09.009.

[11] L.L. Li, P. Zhang, Z.J. Zhang, Z.F. Zhang, Effect of crystallographic orientation and grain boundary character on fatigue cracking behaviors of coaxial copper bicrystals, Acta Mater. 61 (2) (2013) 425–438, http://dx.doi.org/10.1016/j.actamat.2012.08.045.

[12] Z. Zhang, L. Li, Z. Zhang, P. Zhang, Twin boundary: Controllable interface to fatigue cracking, J. Mater. Sci. Technol. 33 (7) (2017) 603–606, http://dx.doi.org/10.1016/j.jmst.2017.03.022.
[13] X. Song, Y. Wang, J. Zhang, Y. Lu, Y. Wang, Z. Chen, The formation of intragranular stress concentration in plastic deformed Ni-base superalloy: Governing factors and process, Mater. Sci. Eng. A 806 (2021) 140820, http://dx.doi.org/10.1016/j.msea.2021.140820.
[14] W.W. Sun, H. Fang, N.H.v. Dijk, S.v.d. Zwaag, C.R. Hutchinson, Linking surface precipitation in Fe-Au alloys to its self-healing potential during creep loading, Metall. Mater. Trans. B 48 (5) (2017) 2109–2114, http://dx.doi.org/10.1007/s11661-017-4025-x.
[15] J.D. Hu, F.Z. Xuan, C.J. Liu, B. Chen, Modelling of cavity nucleation under creep-fatigue interaction, Mech. Mater. 156 (January) (2021) 103799, http://dx.doi.org/10.1016/j.mechmat.2021.103799.
[16] E.A. West, M.D. McMurtrey, Z. Jiao, G.S. Was, Role of localized deformation in irradiation-assisted stress corrosion cracking initiation, Metall. Mater. Trans. A 43 (1) (2012) 136–146, http://dx.doi.org/10.1007/s11661-011-0826-5.
[17] D. An, T. Griffiths, P. Konijnenberg, S. Mandal, Z. Wang, S. Zaefferer, Correlating the five parameter grain boundary character distribution and the intergranular corrosion behaviour of a stainless steel using 3D orientation microscopy based on mechanical polishing serial sectioning, Acta Mater. 156 (2018) 297–309, http://dx.doi.org/10.1016/j.actamat.2018.06.044.
[18] Z. Zhang, S. Xia, Q. Bai, T. Liu, H. Li, B. Zhou, L. Wang, W. Ma, Effects of 3-D grain boundary geometrical angles and the net normal stress on intergranular stress corrosion cracking initiation in a 316 stainless steel, Mater. Sci. Eng. A 765 (2019) 138277, http://dx.doi.org/10.1016/j.msea.2019.138277.
[19] T. Fujii, T. Sawada, K. Tohgo, Y. Shimamura, Mechanical criterion for nucleation of intergranular stress corrosion cracking in austenitic stainless steel, Forces Mech. 3 (2021) 100013, http://dx.doi.org/10.1016/j.finmec.2021.100013.
[20] G. Reisner, E. Werner, F. Fischer, Micromechanical modeling of martensitic transformation in random microstructures, Int. J. Solids Struct. 35 (19) (1998) 2457–2473, http://dx.doi.org/10.1016/S0020-7683(97)00149-2.
[21] A. Malik, G. Amberg, A. Borgenstam, J. Ågren, Effect of external loading on the martensitic transformation–a phase field study, Acta Mater. 61 (20) (2013) 7868–7880, http://dx.doi.org/10.1016/j.actamat.2013.09.025.
[22] P. Sedmák, J. Pilch, L. Heller, J. Kopeček, J. Wright, P. Sedlák, M. Frost, P. Šittner, Grain-resolved analysis of localized deformation in nickel-titanium wire under tensile load, Science 353 (6299) (2016) 559–562, http://dx.doi.org/10.1126/science.aad6700.
[23] D.M. Saylor, B.S. El-Dasher, B.L. Adams, G.S. Rohrer, Measuring the five-parameter grain-boundary distribution from observations of planar sections, Metall. Mater. Trans. A 35 (2004) 1981–1989, http://dx.doi.org/10.1007/s11661-004-0147-z.
[24] K. Maruyama, Effect of plastic strain incompatibility on 0.1% proof stresses of zinc bicrystals, Trans. Jpn. Inst. Met. 22 (No.10) (1981) 723–732, http://dx.doi.org/10.2320/matertrans1960.22.723.
[25] L. Chingshen, T. Bretheau, The role of grain boundary compatibility in fatigue cracking of aluminum bicrystals, Acta Metall. 37 (10) (1989) 2645–2650, http://dx.doi.org/10.1016/0001-6160(89)90297-6.
[26] T. Richeton, S. Berbenni, Effects of heterogeneous elasticity coupled to plasticity on stresses and lattice rotations in bicrystals: A Field Dislocation Mechanics viewpoint, Eur. J. Mech. A Solids 37 (2013) 231–247, http://dx.doi.org/10.1016/j.euromechsol.2012.06.010.
[27] T. Richeton, I. Tiba, S. Berbenni, O. Bouaziz, Analytical expressions of incompatibility stresses at $\Sigma 3 < 111 >$ twin boundaries and consequences on single-slip promotion parallel to twin plane, Phil. Mag. 95 (1) (2015) 12–31, http://dx.doi.org/10.1080/14786435.2014.984787.
[28] S. El Shawish, T. Mede, Grain boundary stresses in elastic materials, Eur. J. Mech. A Solids 99 (2023) 104940, http://dx.doi.org/10.1016/j.euromechsol.2023.104940.
[29] K. Liu, M.H.F. Sluiter, Stresses at grain boundaries: The maximum incompatibility stress in an infinitely extended elastic bicrystal under uniaxial loading, Scr. Mater. 234 (2023) 115570, http://dx.doi.org/10.1016/j.scriptamat.2023.115570.
[30] M. Kamaya, Y. Kawamura, T. Kitamura, Three-dimensional local stress analysis on grain boundaries in polycrystalline material, Int. J. Solids Struct. 44 (10) (2007) 3267–3277, http://dx.doi.org/10.1016/j.ijsolstr.2006.09.020.
[31] J. Hure, S. El Shawish, L. Cizelj, B. Tanguy, Intergranular stress distributions in polycrystalline aggregates of irradiated stainless steel, J. Nucl. Mater. 476 (2016) 231–242, http://dx.doi.org/10.1016/j.jnucmat.2016.04.017.
[32] S. Zhang, L. Wang, G. Zhu, M. Diehl, A. Maldar, X. Shang, X. Zeng, Predicting grain boundary damage by machine learning, Int. J. Plast. 150 (December 2021) (2022) 103186, http://dx.doi.org/10.1016/j.ijplas.2021.103186.
[33] S.H. Choi, J.C. Brem, F. Barlat, K.H. Oh, Macroscopic anisotropy in AA5019A sheets, Acta Mater. 48 (8) (2000) 1853–1863, http://dx.doi.org/10.1016/S1359-6454(99)00470-X.
[34] P.K.C. Venkatsurya, R.D.K. Misra, M.D. Mulholland, M. Manohar, J.E. Hartmann, The impact of microstructure on yield strength anisotropy in linepipe steels, Metall. Mater. Trans. A 45 (5) (2014) 2335–2342, http://dx.doi.org/10.1007/s11661-014-2257-6.
[35] Z. Zhang, C. Deng, Hydrostatic pressure-induced transition in grain boundary segregation tendency in nanocrystalline metals, Scr. Mater. 234 (2023) 115576, http://dx.doi.org/10.1016/j.scriptamat.2023.115576.
[36] A.G. Every, A.K. McCurdy, Second and higher order elastic constants, in: D.F. Nelson (Ed.), Landolt-Börnstein - Group III, Vol. 29A, Springer-Verlag Berlin Heidelberg, 1992, http://dx.doi.org/10.1007/10046537_19.
[37] J. Gilman, B. Roberts, Elastic constants of TiC and TiB_2, J. Appl. Phys. 32 (7) (1961) 1405, http://dx.doi.org/10.1063/1.1736249.
[38] M. Doraiswami, Elastic constants of magnetite, pyrite and chromite, Proc. Indian Acad. Sci. Sect. A 25 (5) (1947) 413, http://dx.doi.org/10.1007/BF03171417.
[39] R. Chang, L.J. Graham, Low-temperature elastic properties of ZrC and TiC, J. Appl. Phys. 37 (10) (1966) 3778–3783, http://dx.doi.org/10.1063/1.1707923.
[40] H. McSkimin, A. Jayaraman, P. Andreatch Jr., Elastic moduli of GaAs at moderate pressures and the evaluation of compression to 250 kbar, J. Appl. Phys. 38 (5) (1967) 2362–2364, http://dx.doi.org/10.1063/1.1709884.
[41] R. MacFarlane, J. Rayne, C. Jones, Temperature dependence of elastic moduli of iridium, Phys. Lett. 20 (3) (1966) 234–235, http://dx.doi.org/10.1016/0031-9163(66)90340-4.
[42] E. Schreiber, Elastic moduli of single-crystal spinel at 25 °C and to 2 kbar, J. Appl. Phys. 38 (6) (1967) 2508–2511, http://dx.doi.org/10.1063/1.1709937.
[43] M. De Jong, W. Chen, T. Angsten, A. Jain, R. Notestine, A. Gamst, M. Sluiter, C. Krishna Ande, S. Van Der Zwaag, J.J. Plata, et al., Charting the complete elastic properties of inorganic crystalline compounds, Sci. Data 2 (1) (2015) 1–13, http://dx.doi.org/10.1038/sdata.2015.9.
[44] H. Ledbetter, H. Ogi, S. Kai, S. Kim, M. Hirao, Elastic constants of body-centered-cubic titanium monocrystals, J. Appl. Phys. 95 (9) (2004) 4642–4644, http://dx.doi.org/10.1063/1.1688445.
[45] J. Neuhaus, M. Leitner, K. Nicolaus, W. Petry, B. Hennion, A. Hiess, Role of vibrational entropy in the stabilization of the high-temperature phases of iron, Phys. Rev. B 89 (18) (2014) 184302, http://dx.doi.org/10.1103/PhysRevB.89.184302.
[46] P. Smith, C.S. Smith, Pressure derivatives of the elastic constants of potassium, J. Phys. Chem. Solids 26 (2) (1965) 279–289, http://dx.doi.org/10.1016/0022-3697(65)90156-3.
[47] A. Heiming, W. Petry, J. Trampenau, M. Alba, C. Herzig, H. Schober, G. Vogl, Phonon dispersion of the bcc phase of group-IV metals. II. bcc zirconium, a model case of dynamical precursors of martensitic transitions, Phys. Rev. B 43 (13) (1991) 10948, http://dx.doi.org/10.1103/PhysRevB.43.10948.
[48] H.C. Nash, C.S. Smith, Single-crystal elastic constants of lithium, J. Phys. Chem. Solids 9 (2) (1959) 113–118, http://dx.doi.org/10.1016/0022-3697(59)90201-X.
[49] X. Song, Y. Wang, J. Zhang, Y. Lu, Y. Wang, Z. Chen, The formation of intragranular stress concentration in plastic deformed Ni-base superalloy: Governing factors and process, Mater. Sci. Eng. A 806 (2021) 140820, http://dx.doi.org/10.1016/j.msea.2021.140820.
[50] Y. Purohit, S. Jang, D.L. Irving, C.W. Padgett, R.O. Scattergood, D.W. Brenner, Atomistic modeling of the segregation of lead impurities to a grain boundary in an aluminum bicrystalline solid, Mater. Sci. Eng. A 493 (1) (2008) 97–100, http://dx.doi.org/10.1016/j.msea.2007.05.128.
[51] K. Li, B. Tang, M. Zhang, L. Zhao, X. Liu, J. Fan, J. Li, A hydrogen diffusion model considering grain boundary characters based on crystal plasticity framework, Int. J. Plast. 169 (2023) 103740, http://dx.doi.org/10.1016/j.ijplas.2023.103740.
[52] S. Jothi, T.N. Croft, S.G.R. Brown, Influence of grain boundary misorientation on hydrogen embrittlement in bi-crystal nickel, Int. J. Hydrog. Energy 39 (35) (2014) 20671–20688, http://dx.doi.org/10.1016/j.ijhydene.2014.07.020.
[53] D. Raabe, M. Herbig, S. Sandlöbes, Y. Li, D. Tytko, M. Kuzmina, D. Ponge, P.P. Choi, Grain boundary segregation engineering in metallic alloys: A pathway to the design of interfaces, Curr. Opin. Solid. State. Mater. Sci. 18 (4) (2014) 253–261, http://dx.doi.org/10.1016/j.cossms.2014.06.002.
[54] S.I. Ranganathan, M. Ostoja-Starzewski, Universal elastic anisotropy index, Phys. Rev. Lett. 101 (5) (2008) 3–6, http://dx.doi.org/10.1103/PhysRevLett.101.055504.